https://doi.org/10.5194/egusphere-2026-2556
Preprint. Discussion started: 12 June 2026

Hyperspectral camera observations for the determination of aerosol profiles and cloud properties

Erna Frins[1], Thomas Wagner[2], Nicolás Casaballe[1], Sebastian Donner[2], and Steffen Ziegler[2]

[1]Applied Optics Group, Physics Institute, Facultad de Ingeniería, Universidad de la República, Uruguay
[2]Satellite Remote Sensing Group, Max Planck Institute for Chemistry, Mainz, Germany

Correspondence: Erna Frins (efrins@fing.edu.uy) and Thomas Wagner (thomas.wagner@mpic.de)

Abstract. Spectroscopic 2D imaging observations with high temporal resolution are important for the investigation of different atmospheric research topics, e.g. the monitoring of emission plumes from point sources or the radiative effects of rapidly changing cloud fields. Traditional imaging DOAS applications cover one spatial dimension using 2D CCD detectors, while scanning the other dimension by sequentially changing the viewing direction. Several minutes are usually needed to achieve a complete 2D image by such techniques. An alternative with much higher temporal resolution is provided by hyperspectral cameras, which can achieve complete 2D images within a few tens of seconds. The limitations of such observations are sometimes the low spectral resolution (typically a few nanometers) and the rather small field of view (usually covering about $10°$). Nevertheless, hyperspectral cameras were already successfully used from ground based or satellite observations to derive high-resolution spatial patterns of atmospheric trace gases.

In this study we use a hyperspectral camera covering the visible and near IR spectral range ($400 - 1000$ nm) with a spectral resolution of about 4.7 nm. We show that the absorptions of O_4 can be well determined from the measured spectra. We use the derived O_4 absorptions together with the simultaneously measured calibrated radiances to determine atmospheric profiles of the aerosol extinction and cloud properties. Here we exploit one important advantage of the 2D imaging capabilities: the unambiguous distinction between clear and cloudy parts within the recorded image. Such a clear distinction is often impossible from simple 1D elevation scans of typical MAX-DOAS observations.

We derive cloud properties (altitude, horizontal distance and optical depth of scattered clouds) from the 2D images, and aerosol extinction profiles from the spectra of the cloud-free parts of the images. We also investigated potential effects of scattered clouds on the radiation fields between the cloud patches and found that the O_4 absorptions and radiances are not significantly affected by the nearby clouds. This is an important finding for the retrieval of aerosol profiles from MAX-DOAS measurements in partly cloudy sky conditions.

1 Introduction

Multi–AXis Differential Optical Absorption Spectroscopy (MAX–DOAS) measurements are the basis for the determination of height profiles of atmospheric trace gases and aerosol extinction in the lower troposphere below about 2 to 4 km (Platt and Stutz, 2008 and references therein). Typically, MAX–DOAS measurements are performed one-dimensionally, i.e. the scattered

https://doi.org/10.5194/egusphere-2026-2556
Preprint. Discussion started: 12 June 2026

sunlight is observed at a series of elevation angles for a fixed azimuth direction. More sophisticated MAX–DOAS viewing strategies use elevation scans at different azimuth directions or more complex 2D combinations of azimuth and elevation angles (Lohberger et al., 2004; Bobrowski et al., 2006; Heue et al., 2008; Lee et al., 2009; Pikelnaya et al., 2013; Peters et al., 2019). This results in a so–called DOAS image, which is composed of the differential slant column densities (dSCD) of the observed trace gas in different viewing directions. Such measurements usually need a long time for a full image (in the order of minutes to tens of minutes). The downside of using these configurations for obtaining detailed information about the 2D structure of the atmosphere's composition is that they lack an imaging system, since they simply scan a 2D region of space and capture the corresponding spectra of a 2D area, which also requires the assumption that adjacent fields of view do not overlap.

Here we present DOAS imaging measurements with a hyperspectral camera which can be performed within short time periods (~ 35 s). Our hyperspectral 2D DOAS measurements cover a wide spectral range with a limited spectral resolution (see Sect. 2). The instrumental field of view covers $10^\circ \times 8^\circ$ approximately. Vertical profile retrievals usually require elevation angles between about 10° and 30°, which can be covered by combining multiple hyperspectral images. Such high elevation angles are especially important to constrain the vertically integrated trace gas and aerosol amounts in the troposphere. In this study we focus on the analysis and interpretation of the atmospheric oxygen dimer $O_2{-}O_2$ absorption with respect to aerosols and clouds (in this work we will refer to the oxygen dimer as O_4). We also make use of the radiances with absolute calibration, which in some cases is also an advantage compared to typical MAX–DOAS measurements.

The data analysed in this study were acquired in 2018 and 2019 from the rooftop of the institute in Montevideo, Uruguay ($34^\circ 55' 06''$ S, $56^\circ 10' 00''$ W). In most cases, the images were acquired with clear skies or with some scattered clouds in the field of view. The measured radiance and O_4 absorptions are compared to Monte-Carlo radiative transfer simulations in order to constrain the aerosol and cloud properties. For the determination of the cloud properties, the 2D imaging capabilities of the camera measurements are especially important, because the location of the (broken) clouds can be easily identified (which is often not unambiguously possible for normal (1D) MAX-DOAS measurements).

Finally, we investigate the effects of broken clouds on the radiation fields besides them, and their potential influence on the aerosol profile retrievals. The paper is organized as follows: Sect. 2 introduces the hyperspectral camera, and in Sect. 3 the details of the spectral analysis are discussed. Section 4 describes the radiative transfer simulations. The comparison between measurements and simulations are presented and discussed in Sect. 5. Conclusions are provided in Sect. 6.

2 Hyperspectral camera

In this work the spectra of scattered sunlight were recorded using the hyperspectral camera SOC 710-VP, Surface Optics Corp. (see Fig. 1). It is a portable imaging system to acquire spectral image cubes with the help of a line-scanner that scans the image plane created by a lens conforming to a push-broom system. The camera's technical specifications are presented in Table 1. The radiometric calibration was performed by the manufacturer for different aperture settings of the optical system, according to different F-numbers. Depending on the scene and the illumination, we can select F-numbers between 2.8, 5.6 and 11, for which the corresponding radiometric calibrations are available. Our data was acquired using F-number 11.

https://doi.org/10.5194/egusphere-2026-2556
Preprint. Discussion started: 12 June 2026

Table 1. Technical specifications of the hyperspectral camera SOC 710 VP.

Spectral range	400-1000 nm
Spectral Resolution	~ 4.7 nm
Spectral bands	128
Dynamic range	12 bits
Exposure time	$10 - 103$ ms
Pixels per image	696×520
Min. time/ cube	~ 23 s
Lens	35 mm, C-Mount
Weight	2.95 kg

Before collecting the data, a so–called focus camera is moved in front of the lens to focus on the scene, ensuring that the image generated by the scanning camera is also in focus. The scene sweep time depends on the integration time. Scanning the image can take from a few seconds to a little more than a minute. The image cubes in this study were generated in ~ 35 s. The scanning process generates an image cube composed of 128 images acquired at wavelengths between 400 and 1000 nm, each with 696 pixels per line and 520 pixels per column. The spectral resolution is ~ 4.7 nm.

The hyperspectral camera captures an image in which objects and their respective spectra can be clearly identified. The image shown in Fig. 2 is an example of an image recorded with the hyperspectral camera on 11 January 2019, 10:15 LT in Montevideo. Figure 2(a) shows an RGB image and Fig. 2(b) shows the radiance at 550.8 nm. The camera software allows to view and record the image cube and the spectra of any pixel using the cursor. In this example, we indicate three positions in Fig. 2(a) and their corresponding spectra in Fig. 2(c). Pixel (i) is from a sky region, pixel (ii) is over the water (Río de la Plata) and pixel (iii) is from vegetation (trees).

3 DOAS Analysis

The radiance spectra were analyzed using differential absorption optical spectroscopy (DOAS) (Hönninger et al., 2004; Wittrock et al., 2004; Platt and Stutz, 2008; Hendrick et al., 2014). The absorptions in each spectrum were simultaneously fitted to a set of absorption cross sections of trace gases and the logarithm of a Fraunhofer reference spectrum (FRS). To speed up all the analysis we divide the image cubes into boxes of 24×20 pixels and add their spectra together, obtaining new image cubes of 29×26 binned pixels with the same number of wavelength channels. The included trace gases are those relevant in the selected spectral window (see Table 2). The FRS is taken from a measurement in zenith direction. The result of the spectral analysis are the differential slant column densities (dSCD), which are the differences between the integrated trace gas concentrations along the atmospheric light path (SCD) at a specific elevation angle and that of the FRS. For this study we perform the DOAS analysis using the QDOAS software developed at the BIRA-IASB (Fayt and Roozendael, 2001; Danckaert et al., 2017). We used python scripts for pre-processing the hypercube files and prepare the spectra for their DOAS retrieval in QDOAS.

https://doi.org/10.5194/egusphere-2026-2556
Preprint. Discussion started: 12 June 2026

Figure 1. Hyperspectral camera on the rooftop of the institute looking towards the Rio de la Plata in western direction.

Table 2. DOAS fit settings.

Molecule	**Temperature**	**Reference**
O_4	298 K	Hermans et al. (2011)
O_2	203 K	Bogumil et al. (2003)
NO_2	294 K	Vandaele et al. (1998)
O_3	293 K	Burrows et al. (1999)
Water vapour	293 K	Rothman et al. (2013)
Analysis window		$400 - 660$ nm
Polynomial order		5

We focus on the analysis of O_4 dSCDs, for which the spectral range $400 - 660$ nm was used. The strongest O_4 absorption band in this spectral range is at 577 nm. We performed sensitivity tests to optimise the DOAS fitting settings and quantified the uncertainties of the derived O_4 dSCDs. We varied the spectral range, used different optionns for the FRS and tested the impact of using radiometrically calibrated spectra, fitting a Ring spectrum (Chance and Spurr, 1997) or including an intensity offset in the DOAS fit. The details of these sensitivity studies are presented in the Appendix A. The final selected optimised fit settings are presented in Table 2. An example of a fit result is shown in Fig. 3, comparing the effect of including or omitting the O_2 cross section in the DOAS retrieval.

https://doi.org/10.5194/egusphere-2026-2556
Preprint. Discussion started: 12 June 2026

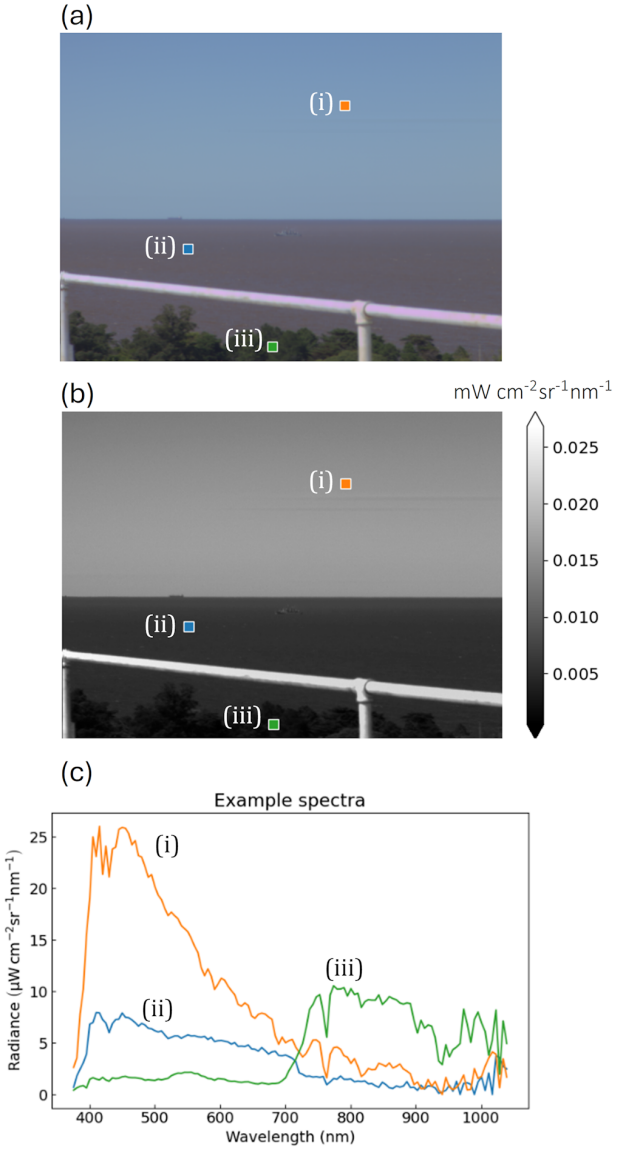

Figure 2. Example of an image cube acquired on 11 January 2019, 10:15 LT with the hyperspectral camera. Panel (a) shows the RGB image and panel (b) the radiance at 550.8 nm. The spectra of pixels selected over (i) the sky, (ii) the water (Río de la Plata river) and (iii) the trees are plotted in panel (c).

4 Radiative transfer simulations

For the simulations of the observed absolute radiance (in units of $\mathrm{mW\,cm^{-2}\,sr^{-1}\,nm^{-1}}$) and the retrieved O_4 dSCDs we use two Monte-Carlo radiative transfer models. MCARTIM v1 (Deutschmann et al., 2011) is applied for the 1D-simulations. Only vertical gradients of atmospheric properties can be used as input in this program. For the 3D–simulations (including also

https://doi.org/10.5194/egusphere-2026-2556
Preprint. Discussion started: 12 June 2026

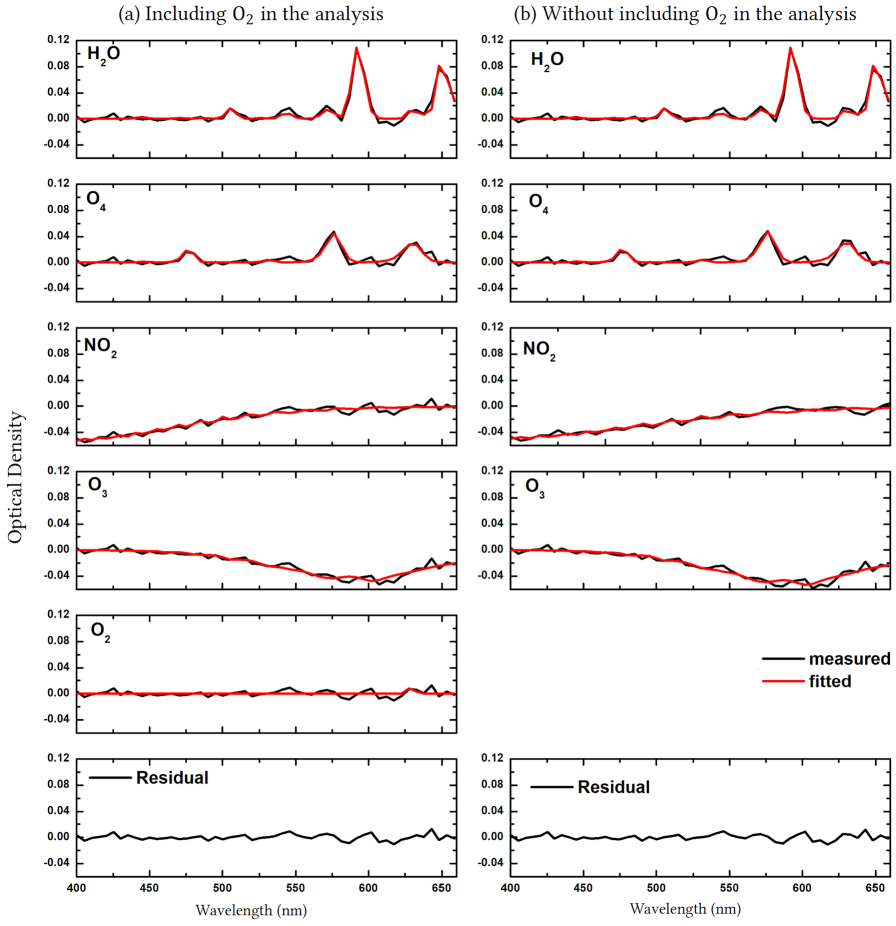

Figure 3. Example of a DOAS analysis for a selected spectrum acquired on 1 November 2018, 15:54 LT and zenith at 17:05 LT including and not including the O_2 molecule (panels (a) and (b), respectively). In the first case, the dSCD for water vapour and the oxigen dimer are $(2.16 \pm 0.08) \times 10^{23}$ molec. cm^{-2} and $(4.5 \pm 0.4) \times 10^{43}$ molec.^{2} cm^{-5}, respectively; the RMS is 4.39×10^{-3}. When the oxygen molecule was not included in the analysis the dSCDs for water vapour and the oxygen dimer are $(2.16 \pm 0.08) \times 10^{23}$ molec. cm^{-2} and $(4.8 \pm 0.4) \times 10^{43}$ molec.^{2} cm^{-5}, respectively; the RMS is slightly increased to 4.50×10^{-3}.

horizontal gradients) we use TRACY-2 (Wagner et al., 2007, 2023). Both models show identical results for 1D simulations, although TRACY-2 is much slower than MCARTIM.

The simulations were carried out for a wavelength of 577 nm, which matches the wavelength of the strongest O_4 absorption band in the spectral range used in the DOAS analysis. For simplicity, the radiance output at that wavelength was also used for the comparison to the measured radiances at 571 nm. For the cases considered in this study (including considerable amounts of aerosols), the effect of this small wavelength difference between measurements and simulations is negligible (below 1%).

TRACY-2 and MCARTIM yield radiances normalised against the solar irradiance. For the calculation of absolute radiances, we convolved the solar irradiance spectrum from Chance and Kurucz (2010) with a Gaussian slit function with full width at

https://doi.org/10.5194/egusphere-2026-2556
Preprint. Discussion started: 12 June 2026

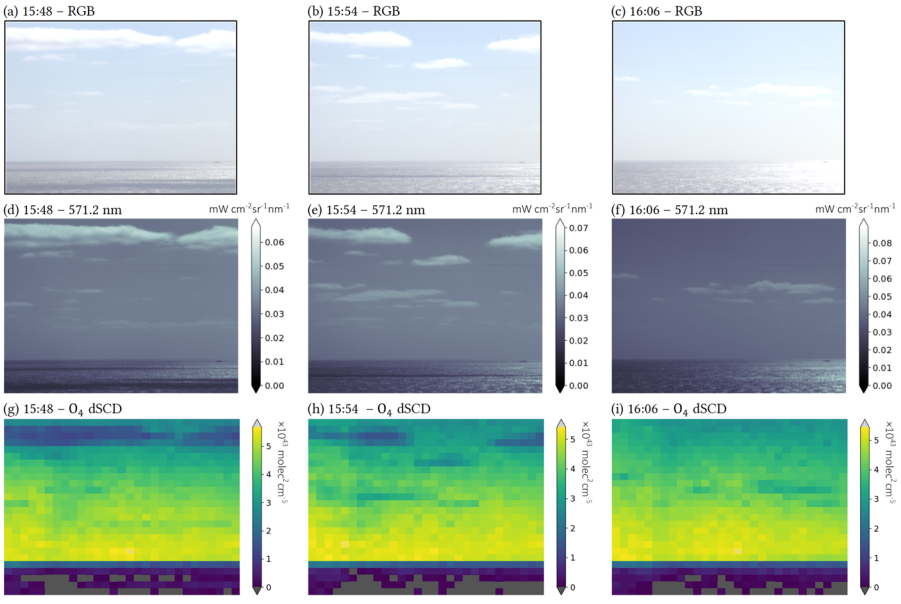

Figure 4. RGB images (panels a-c), 2D radiances at 571.2 nm (panels d-f) and the absorption of O_4 (panels g-i) analyzed in the $400-660$ nm spectral window (see Sect. 3) for image cubes acquired on 1 November 2018 with broken clouds in the field of view. To speed up the DOAS analysis, the original 696×520 spatial resolution was reduced to 29×26 binned pixels.

half maximum (FWHM) of 4.7 nm. The convolved irradiance at 571 nm ($1.83 \mathrm{W\,m^{-2}\,nm^{-1}}$) is then multiplied with the output from the radiative transfer models to obtain absolute radiance values. The O_4 SCDs are calculated from the simulated O_4 AMFs by multiplication with the O_4 VCD (1.34×10^{43} molec.^{2} cm^{-5}) derived from atmospheric temperature and pressure profiles (see details in Table 3). Finally, the O_4 SCD of the zenith spectrum is subtracted from the O_4 SCDs of the low elevation measurements to obtain the O_4 dSCDs corresponding to the output of the DOAS analysis.

The input parameters considered in the radiative transfer simulations and their sources are summarised in Table 3. It should be noted that the temperature and pressure profiles are extrapolated from the surface values of temperature, pressure and relative humidity. Thus, these profiles do not exactly represent the true profiles, especially at higher altitudes. However, since our measurements are most sensitive to the lowest part of the atmosphere the corresponding uncertainties are not critical.

For the calibration of the elevation angles of the camera, the measured radiances and retrieved O_4 dSCDs are compared to radiative transfer simulations (Fig. 5). Below about $-0.1°$ both quantities strongly decrease indicating the transition of the bright sky to the darker water surface (outside the sun glint region at the right side of the camera images). From the simulation results, we estimate the effective horizon to be at around $-0.3°$, corresponding to about the 5th camera row from the bottom.

https://doi.org/10.5194/egusphere-2026-2556
Preprint. Discussion started: 12 June 2026

Table 3. Input parameters used for the radiative transfer simulations.

Parameter	Value(s)	Source
SZA	49.1°, 50.4°, 52.8°	Calculation based on the location and measurement times of the three selected spectra (Fig. 4).
Azimuth angle of the center of the camera	270° (west)	Camera alignment.
Relative azimuth angles (RAA) for left edge, center, and right edge of the camera	Left edge: 6.5°, 5.5°, 3.4° Center: 11.5°, 10.5°, 8.4° Right edge: 16.5°, 15.5°, 13.4°	Calculation according to the properties of the camera.
Elevation angles	-1.89° -1.13° -0.36° 0.02° 0.41° 1.17° 1.94° 2.71° 3.47° 4.24° 5.00° 5.77° 6.54° 7.69°	Calculation according to the properties of the camera, in combination with the 'elevation scan' (see Fig. 5 and text).
Field of view (FOV)	$0.38^\circ \times 0.33^\circ$	FOV of each binned camera pixel.
Altitude of instrument	~ 50 m	Height of building above sea level.
O_3 profile	US standard atmosphere, scaled with O_3 VCD of 330 DU	O_3 VCD from OMI satellite observations, available at the TEMIS web site (https://www.temis.nl).
Surface albedo	5%, 20%, 25% (Lambertian surface)	Constrained by the measured radiance and O_4 absorption, see text.
Profiles of temperature, pressure and relative humidity	Extrapolated from surface values ($14\,^\circ$C, 1018 hPa, 55%)	Obtained from measurements at the airport Carrasco, about 20 km away from the measurement site. The surface temperature was extrapolated up to 12 km altitude, assuming a lapse rate of 6.5 K km^{-1}. Above 12 km it was assumed to be constant. The pressure profile was calculated from the temperature profile.
O_4 profile	Square of O_2 concentration	Calculated from temperature and pressure profiles assuming a relative humidity of 55 %.
Aerosol extinction profile	Various assumed profiles	Constrained by measured radiance and O_4 absorption, see text.
Aerosol asymmetry parameter	0.60, 0.68, 0.75, 0.85	Constrained by measured radiance and O_4 absorption, see text.
Aerosol single scattering albedo	0.95, 1.00	Constrained by measured radiance and O_4 absorption, see text.

https://doi.org/10.5194/egusphere-2026-2556
Preprint. Discussion started: 12 June 2026

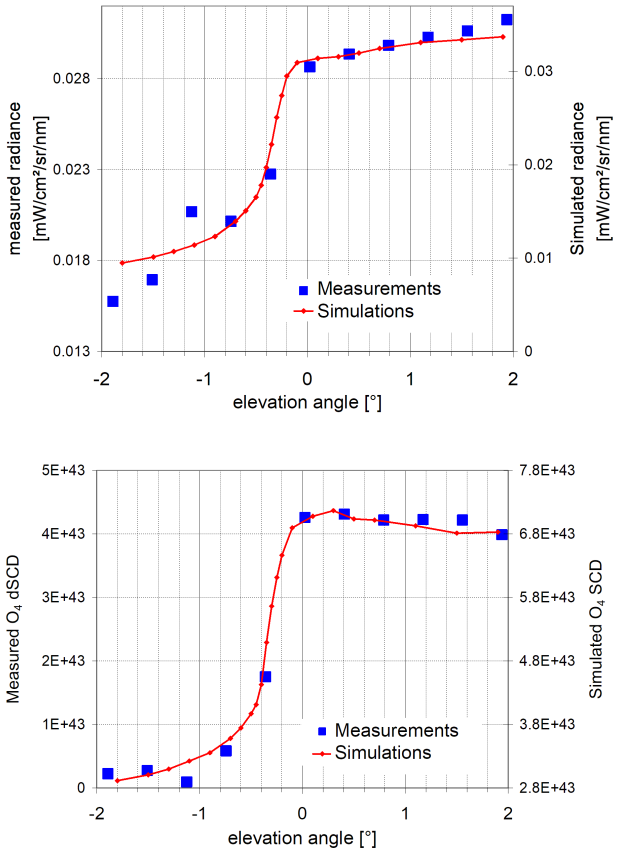

Figure 5. Dependence on the elevation angle of the measured and simulated radiances at 571 nm (top) and the O_4 SCDs at 577 nm (bottom) on 1 November 2018, 15:48 LT. The blue squares represent the measurements for the lowest eleven (binned) detector pixels at the left edge of the image (outside the region of strong sun glint).

5 Comparison to measurements

For the comparison between measurements and simulations, three measurements on 01 November 2018 were selected (see Fig. 4). During these measurements the sky was mainly clear, but also partly covered with few clouds. These conditions are ideal to investigate both the influence of aerosols and clouds on the camera measurements. In the next sub-sections, first the aerosol extinction profiles are constrained using the measurements in the cloud-free regions. Then the properties of clouds are determined taking into account the derived aerosol profiles in the previous step. Finally, the influence of broken clouds on the atmospheric radiation field is investigated. The comparisons are made for the binned results with 26 pixels in the vertical and 29 pixels over the horizontal dimension.

https://doi.org/10.5194/egusphere-2026-2556
Preprint. Discussion started: 12 June 2026

5.1 Determination of aerosol extinction profile

For the determination of the aerosol profiles, we did not apply a routine MAX–DOAS inversion method, because of two reasons. First, the elevation angle range covered by the camera is much smaller ($< 8°$) than for typical MAX-DOAS measurements. Thus, the upper part of the aerosol extinction profile cannot well be constrained by the O_4 measurements. Second, we also used the radiance measurements for the determination of the aerosol extinction profiles, which is especially advantageous, because the radiance measurements of the camera are absolutely calibrated. Considering the radiance measurements together with the O_4 dSCDs for the determination of the aerosol extinction profiles allows to constrain the total AOD and thus also the upper part of the aerosol extinction profile.

Our approach to constrain the aerosol extinction profiles was to assume a variety of possible aerosol extinction profiles and use them as input into the radiative transfer model. Then, the simulated radiances and O_4 dSCDs are compared with the corresponding measured quantities. By varying the surface albedo and fundamental properties of the aerosol profiles (shape and total AOD) and subsequent comparison of the simulation results to the measurements, the following basic conclusions could be drawn:

a) the aerosol extinction close to the surface has to be relatively small ($< 0.1\ \mathrm{km}^{-1}$) to match the measured O_4 dSCDs. Here it is important to note that we applied a scaling factor of 0.8 to the measured O_4 dSCDs (Ortega et al., 2016; Wagner et al., 2019, 2021 and references therein). If no scaling factor is applied, the measured O_4 dSCDs can also be matched by the simulations, but only for a rather high surface albedo (see Appendix B).

b) the total AOD has to be rather high (about 0.2 or higher) to match the measured radiances. Together with the first finding, this suggests that a considerable fraction of the aerosol extinction occurs at elevated layers. Thus, in the following we assume an aerosol profile with two layers: one layer close to the surface ($< 1\ \mathrm{km}$), which is mostly constrained by the O_4 dSCDs, and a second layer at higher altitude ($> 3\ \mathrm{km}$), which is mostly constrained by the radiance measurements.

c) If a low surface albedo (e.g., 0.05) is used in the simulations, the measured radiances cannot be matched by the simulations, unless a rather high surface albedo (0.2 or more) is assumed. This finding was unexpected, because usually the albedo of water in the visible spectral range is rather low. The need for a high surface albedo can be explained by the specific viewing geometry of our measurements and the strong forward scattering probability of aerosol scattering. As seen in the camera images (Fig. 4), the recorded brightness of the sea surface (especially in the right parts of the images) is rather high, due to the specular reflection of the sun light (sun glint), because the relative azimuth angle (RAA) between the viewing direction and the sun position was rather small (around $10°$). Because of the small RAA, also the probability of aerosol scattering of light from the sun and from the sun glint region into the field of view of the instrument is rather high. But the corresponding enhancement of the observed sky radiance close to the horizon cannot be well described by the Lambertian surface reflection model used in the radiative transfer models. In order to compensate this deficiency, an increased albedo has to be used to match

https://doi.org/10.5194/egusphere-2026-2556
Preprint. Discussion started: 12 June 2026

The best matching aerosol extinction profiles found with this procedure are shown in Fig. 6(a) and 6(b). The simulation results are obtained for the viewing geometry of the center column of the camera image, while the measurements represent all 29 columns (elevation scans) of the camera. The extinction values close to the surface are similar for both profiles, but the altitude ranges of the second layer are slightly different. The measured and simulated O_4 dSCDs and radiances are compared in Fig. 6(c) and 6(d). For the measurements above the horizon, good agreement between measurements and simulations is found. The variation of the measurements for the different azimuth directions (from left to right of the camera image) is relatively small.

For the elevation angles below the horizon, the agreement is worse, especially for the radiances. In particular, the dependence of the measured radiances on the azimuth angle is rather high. These findings are caused by the effect of the specular reflection of sun light (sun glint) discussed above. Specular reflection of sun light is not included in the radiative transfer simulations.

The simulations are made for the following aerosol properties: single scattering albedo (SSA): 1.0, asymmetry parameter (AP): 0.68. For other choices of these optical properties worse agreement is found. Possibly, other phase function parametrizations might lead to a better agreement.

The existence of an aerosol profile with two layers might be explained by different sources: close to the river surface the aerosols are possibly sea spray aerosols. Although the viewing direction of the measurements is towards the Río de la Plata, especially during summer often salt water is entrained into that river (the sea breeze in the afternoon is a standard phenomenon at Montevideo). The second aerosol layer at higher altitudes might be caused by long range transport from sources in Argentina (Buenos Aires is about $200\ \mathrm{km}$ away in viewing direction of the instrument). Back trajectory simulations support this interpretation (see Appendix C).

Similar results are found for other measurements of the same day, see Fig. 7. There also the effect of the varying relative azimuth angle (from the right to the left side of the image) is considered in the radiative transfer simulations.

Overall, good agreement is again found. The effect of the relative azimuth angle is rather small for the simulated radiances and negligible for the O_4 dSCDs. Interestingly, for the later measurements, the simulated radiances tend to underestimate the measured radiances. This is probably caused by the decreasing RAA, which further increases the influence of sun glint.

As a general conclusion, we find that the simulations for the selected aerosol profiles agree well to the three camera measurements of the selected day.

5.2 Determination of cloud properties

In this section, the influence of clouds on the measured quantities is investigated. For the radiative transfer simulations, the aerosol profile A derived in the previous section is used. In addition, 3D cloud structures are included in the radiative transfer simulations.

The measurements on 1 November 2018, 15:48 LT are used to investigate the effect of clouds because, in the corresponding image, bright clouds are seen close to the upper edge of the image and, also, a portion of clear sky between these clouds exists. The effect of these clouds is clearly visible in Fig. 6, where the O_4 dSCDs show a minimum and the radiances show a maximum at elevation angles around 7°.

https://doi.org/10.5194/egusphere-2026-2556
Preprint. Discussion started: 12 June 2026

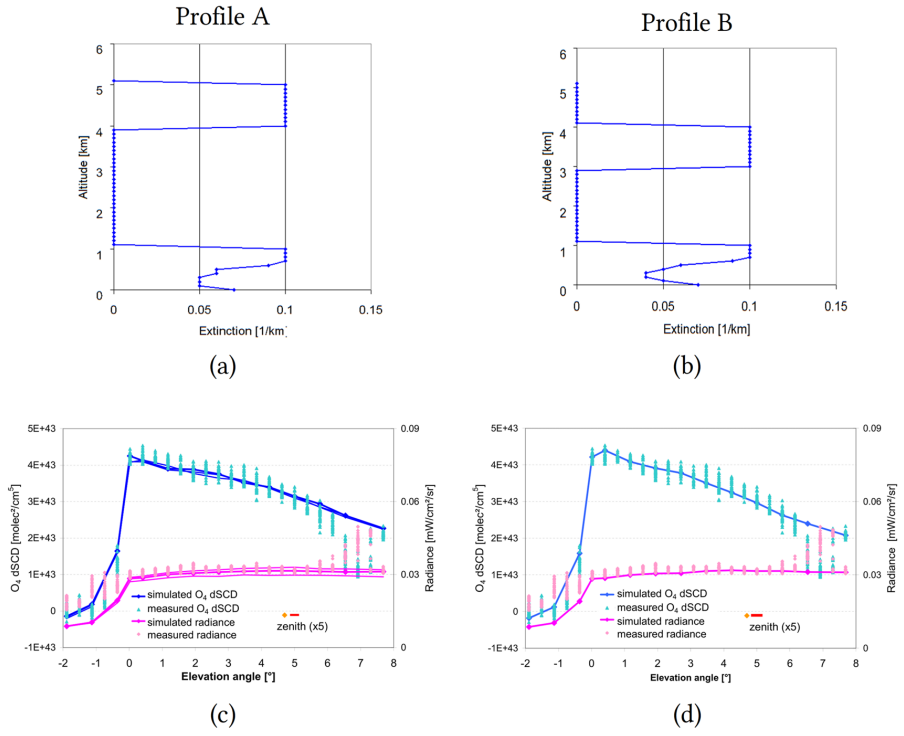

Figure 6. (a, b): two aerosol extinction profiles, for which the best agreement between measurements and simulations are found. (c, d): comparison of the measured and simulated radiances and O_4 dSCDs. The blue and magenta dots show the measured values of the 29 vertical scans of the measurements on 01 November 2018, 15:48 (LT). The blue and magenta lines show the corresponding results of the simulations (for the vertical scan in the center of the camera). Also shown are the measured and simulated radiances (indicated by the orange diamond and red bar, respectively) in zenith direction (note that these values are multiplied by 5 to make them better visible. Clouds are not considered in the simulations. Thus, the simulation results deviate from the measurements at around 7° elevation, which are affected by clouds.

We assumed different 3D cloud structures in the radiative transfer simulations in order to match both the measured radiances and O_4 dSCDs. In a first step, the extinction and size of the cloud is varied until the simulations match the measured radiances. Clouds at different horizontal distances (and altitudes) can fulfill this condition (the ratio between distance and altitude is fixed by the elevation angles at which the cloud effects appear). For an elevation angle of 7°, the ratio between the altitude and distance is about 0.12. We made simulations for clouds at three distances: 5, 10, and 15 km. The cloud properties, which best match the observed radiances are shown in Table 4. Here it is interesting to note that for the cloud at 15 km distance a higher integrated extinction had to be assumed than for the clouds at shorter distances in order to match with observations. Otherwise, the observed radiance was underestimated by the simulations. The increased integrated extinction (and thus reflectance of the cloud) compensates the increased light extinction between the cloud and the instrument due to Rayleigh and aerosol scattering.

In the second step, the simulated O_4 dSCDs for the clouds at different horizontal distances are compared to the measured O_4 dSCDs (see Fig. 8).

https://doi.org/10.5194/egusphere-2026-2556
Preprint. Discussion started: 12 June 2026

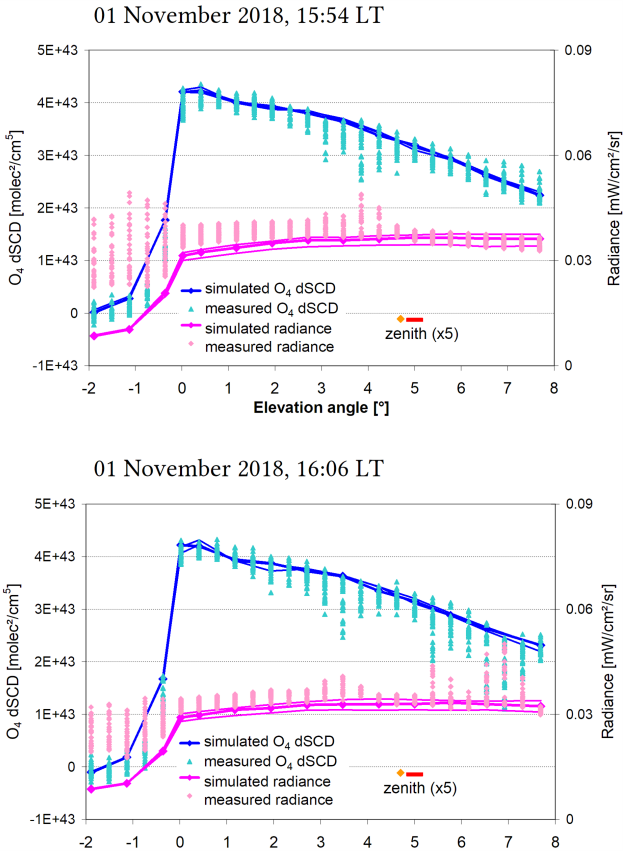

Figure 7. Comparison between measured and simulated radiances and O_4 dSCDs for the two following measurements on 01 November 2018 (see Fig. 4). For the simulations the aerosol extinction profile A (see Fig. 6) is used. The simulations are made for three different relative azimuth angles corresponding to the center and the right and left edges of the camera images. Also shown are the measured simulated radiances (indicated by the orange diamond and red bar, respectively) in zenith direction (note that these values are multiplied by 5 to make them better visible).

Table 4. Cloud properties assumed for the 3D radiative transfer simulations.

distance between the instrument and clouds	altitude of the cloud	horizontal extent along / across viewing direction	vertical extent	extinction
5 km	600 – 650 m	500 m / 1000 m	50 m	30 km^{-1}
10 km	1200 – 1300 m	500 m / 1000 m	100 m	15 km^{-1}
15 km	1900 – 2050 m	500 m / 1000 m	150 m	15 km^{-1}

https://doi.org/10.5194/egusphere-2026-2556
Preprint. Discussion started: 12 June 2026

While for all scenarios the measured radiances are matched by the simulations, agreement for the O_4 dSCDs is only found for a cloud at around $10\ \mathrm{km}$ distance. Although this comparison is based on rather simple assumptions, we can conclude that the 2D information from the camera images together with 3D radiative transfer simulations allow to determine the distance and altitude of broken clouds.

5.3 Influence of broken clouds on the radiation field and aerosol retrievals in the vicinity of a broken cloud

In this section we investigate how broken clouds in the field of view of the instrument influence the radiation field close to them, and how they potentially affect the MAX–DOAS profile retrievals. For that purpose, we again selected the viewing geometry of the measurements on 01 November 2018, 15:54 LT (see Fig. 8). We performed simulations for two scenarios, one with a broken cloud in the field of view (case 2 in Table 4), and one without the cloud. Three azimuth angles were chosen: one in the direction of the center of the cloud, and two directions directly besides the cloud at $\pm 3.1^\circ$ compared to the central azimuth direction. For these azimuth angles, the lines of sight are very close to the edges of the cloud with horizontal distances of about $15\ \mathrm{km}$.

The results for both scenarios are shown in Fig. 9. Almost identical results are found for the scenarios with and without the cloud. Slight differences are found for the radiances (but not for the O_4 dSCDs) close to the horizon, which are caused by the cloud shadow.

These findings indicate that broken clouds (as used in our simulations) have no significant influence on MAX–DOAS observations close to cloud edges. This is an important result for MAX–DOAS analyses in broken cloud conditions because it can be concluded that in the presence of broken clouds, aerosol profile retrievals are still possible using the clear sky observations between the clouds.

Imaging DOAS measurements have an important advantage compared to usual MAX–DOAS observations (scanning only in one azimuth direction), because from 2D images the cloudy parts of the sky can be well and unambiguously determined, which is often not possibly for 1D MAX–DOAS observations.

6 Conclusions

We performed and analysed spectroscopic 2D imaging observations using a hyperspectral camera on two days in Montevideo, Uruguay. The camera covers the visible and near-IR spectral range ($400 - 1000\ \mathrm{nm}$) with a spectral resolution of about $4.7\ \mathrm{nm}$ FWHM. The main advantage of such 2D imaging measurements compared to the 'classical' imaging DOAS is the high temporal resolution of only a few tens of seconds. Thus, quasi–instantaneous 2D measurements of atmospheric constituents can be achieved.

In this study we analysed the atmospheric absorptions of the oxygen dimer. From the latter we derived aerosol and cloud properties from the recorded images which cover a field of view of about $10^\circ \times 8^\circ$ in horizontal and vertical directions, respectively. For the determination of the aerosol extinction profiles, we also used the absolutely calibrated measured radiances. In

https://doi.org/10.5194/egusphere-2026-2556
Preprint. Discussion started: 12 June 2026

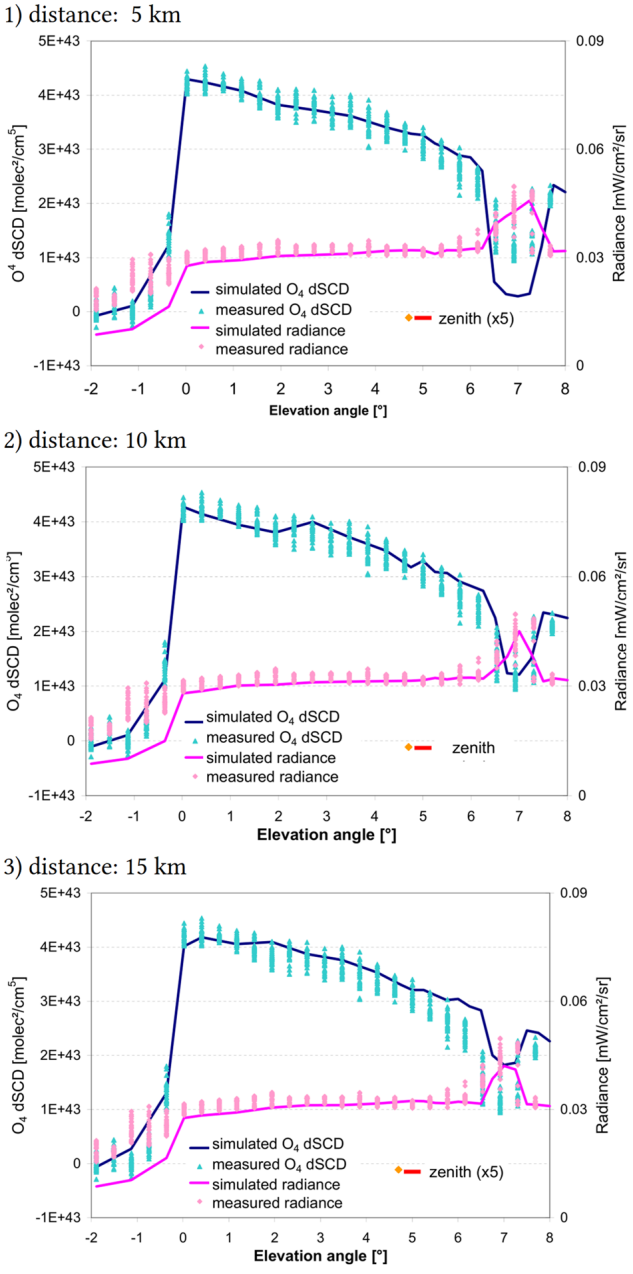

Figure 8. Comparison between the measured and simulated radiances and O_4 dSCDs for clouds at different distances (and altitudes, see Table 4). Also shown are the measured and simulated radiances (indicated by the orange diamond and red bar, respectively) in zenith direction (note that these values are multiplied by 5 to make them better visible).

https://doi.org/10.5194/egusphere-2026-2556
Preprint. Discussion started: 12 June 2026

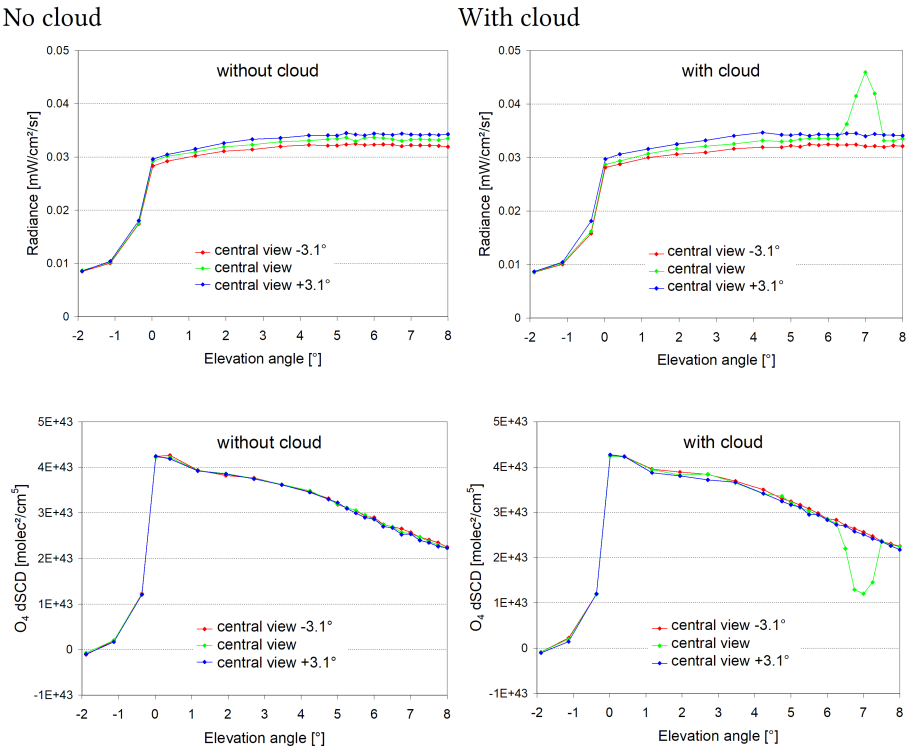

Figure 9. Comparison of radiances and O_4 dSCDs for scenarios with and without a cloud in the elevation scan of the central viewing direction. In addition to the central viewing direction, also results for azimuth angles at the clear sky parts at both sides of the cloud ($\pm 3.1°$) are shown. The SZA and sun azimuth angle are as for the camera measurement on 01 November 2018, 15:54 LT. The cloud is located at 10 km distance from the instrument (second case in Table 4).

that way it was possible to constrain the total AOD even without measurements at intermediate elevation angles ($\sim$ 10 to 30°), which are usually included in MAX–DOAS profile inversions.

One important advantage of the 2D imaging capabilities of the hyperspectral camera is clear and cloudy parts within the recorded image can be unambiguous identified. Such a clear distinction is often impossible from simple 1D elevation scans of typical MAX–DOAS observations. We derived aerosol extinction profiles from the spectra of the cloud free parts of the 2D images, and the cloud properties (altitude, horizontal distance and optical depth of scattered clouds) from the cloudy parts of the 2D images. From our 2D observations, we also investigated the potential effects of scattered clouds on the radiation fields between the cloud patches and found that the O_4 absorptions and radiances are not significantly affected by the nearby clouds. This is an important finding for the retrieval of aerosol profiles from MAX–DOAS measurements in partly cloudy sky conditions and within cloud holes.

Future measurements should extend measurements of aerosol and cloud properties for additional measurement conditions including cases with varying cloud fractions and cloud altitudes. Of particular interest could also be cases with optically thick

https://doi.org/10.5194/egusphere-2026-2556
Preprint. Discussion started: 12 June 2026

clouds, which can cause very long light paths inside the clouds due to multiple scattering. From 2D imaging measurements of the O_4 absorption (and also the O_2 absorption), the spatio-temporal heterogeneity of the light paths could be derived.

Another interesting application of the 2D hyperspectral camera could be the measurement of NO_2 patterns in emission plumes from point sources (Manago et al., 2018). Recently, Borger et al. (2025) showed that the horizontal patterns of NO_2 plumes from point sources could be well retrieved from hyperspectral satellite measurements with an even coarser spectral resolution ($\sim 6.5\mathrm{nm}$). We will apply our hyperspectral camera for similar measurements from ground.

Data availability. The data that support the findings of this research are available from the corresponding author upon reasonable request.

Appendix A: Tests on DOAS fit settings

In this appendix we show the results of several tests performed to determine the optimal settings for the DOAS fit, considering the specific characteristics of the hyperspectral camera. Because each of the measurements carries a large amount of information, we first performed some data reduction to speed up the optimization process.

Each image cube consists of 696×520 spectra totalizing 361920 spectra. For the analysis in this study, we cluster the spectra of nearby pixels, reducing the spatial resolution but improving the signal-to-noise ratio. Recall that we divide the image cubes into boxes of 24×20 pixels and add their spectra together, obtaining new image cubes of 29×26 binned pixels with the same number of wavelength channels. In Table A1 we list the DOAS fitting parameters for the O_4 analysis that were varied. We ran our tests on the image cubes acquired on 11 January 2019, 10:11 LT in Montevideo, that captures a clear-sky scene next to a water surface (Río de la Plata). The Fraunhofer reference spectrum image cube (FRS) is a clear-sky scene acquired at 10:05 LT by pointing the hyperspectral camera towards the zenith. The radiances at $550.8\ \mathrm{nm}$ of both image cubes are shown in Fig. A1.

The nominal spectral resolution of the hyperspectral camera is approximately $4.7\ \mathrm{nm}$ according to the manufacturer. To verify this, we performed DOAS retrievals varying the spectral resolution of the fitted reference spectra from $4.3\ \mathrm{nm}$ to $5.1\ \mathrm{nm}$ (see Table A1). A representative example of the tests carried out on one binned pixel of the image cube is presented in Fig. A2. The trace gas absorptions of water vapour and the oxygen dimer in the measured spectrum are quite strong and match well with the fitted absorption cross sections. In contrast, the amplitude of the fitted Ring spectrum is almost negligible.

We use the relative fit error of the O_4 dSCD in different configurations to select the optimal DOAS analysis configuration. Figure A3(a) shows the interquartile ranges and medians of the relative errors of the sky pixels of the considered image cube for the various fit configurations.

The distributions of the relative errors are similar to each other in most scenarios, except for the $400 - 610\ \mathrm{nm}$ spectral window. Thus, the configurations using this window were excluded in Fig. A3(b). According to these distributions, the lowest overall relative error is found when using a gaussian slit function with FWHM between 4.7 and $5.1\ \mathrm{nm}$ for all the configura-

https://doi.org/10.5194/egusphere-2026-2556
Preprint. Discussion started: 12 June 2026

Table A1. Parameters values used to find the optimal result of the DOAS analysis.

Parameter	
Spectral resolution (nm)	4.3; 4.5; 4.7; 4.9; 5.1
Fitting window (nm)	A: 400 – 660
	B: 400 – 665
	C: 420 – 500
Intensity offset	with / without
Ring spectrum	with / without

tions, but the relative errors show little sensitivity when the slit function varies between 4.5 nm and 4.9 nm. The relative errors for the 4.7 nm case are in fact smaller, which agrees with the nominal resolution value provided by the manufacturer.

Additionally, we studied the impact of including a Ring spectrum or fitting an intensity offset in the DOAS analysis. No significant change of the fit results for O_4, H_2O and O_2 was found in the tests if a Ring spectrum and/or an intensity offset was included or not (see Fig. A2). The low importance of the Ring effect is probably related to the decrease of the Raman scattering probability towards longer wavelengths and to the low spectral resolution of the instrument. Therefore, no Ring spectrum was included in the optimized DOAS analysis configuration. We also found that fitting an intensity offset did not improve the results of the DOAS analysis. On the contrary, there appeared more cases in which the algorithm failed to converge, and with higher relative fitting errors. Therefore, the optimized DOAS analysis configuration does not include the fitting of an intensity offset either. A spectral resolution of 4.7 nm was used for the convolution of the trace gas reference spectra, and the spectra are analysed in a fit window from 400 to 660 nm.

Next, we compared different choices of the reference spectra (FRS) for the DOAS retrievals. In the tests above, individual reference spectra are used in the DOAS analysis for each (binned) camera pixel, taken from the corresponding pixel in the zenith reference image cube. We call this mode of selecting the reference spectra as sequential analysis in the following. Because this scheme is computationally more demanding, we also tested DOAS retrievals using a common, (binned) fixed zenith reference spectrum for the analysis of all pixels of the low elevation measurements.

Although the spectral properties of the camera pixels are very similar, small deviations of these properties between the measured spectra and the zenith reference might lead to degraded fit results. Therefore, we decided to use the sequential analysis for this study.

Finally, we compare in Fig. A4 the retrieved O_4 dSCDs using radiometrically calibrated and non-radiometrically calibrated radiances, both analyzed in sequential mode. The retrievals are not identical; however, the correlation ($R^2 = 0.998$) is very high. The small difference between both retrievals could be due to the fact that the radiometric calibration differs slightly for each spectrum. For the O_4 analysis in this study, we used the radiometrically calibrated spectra.

https://doi.org/10.5194/egusphere-2026-2556
Preprint. Discussion started: 12 June 2026

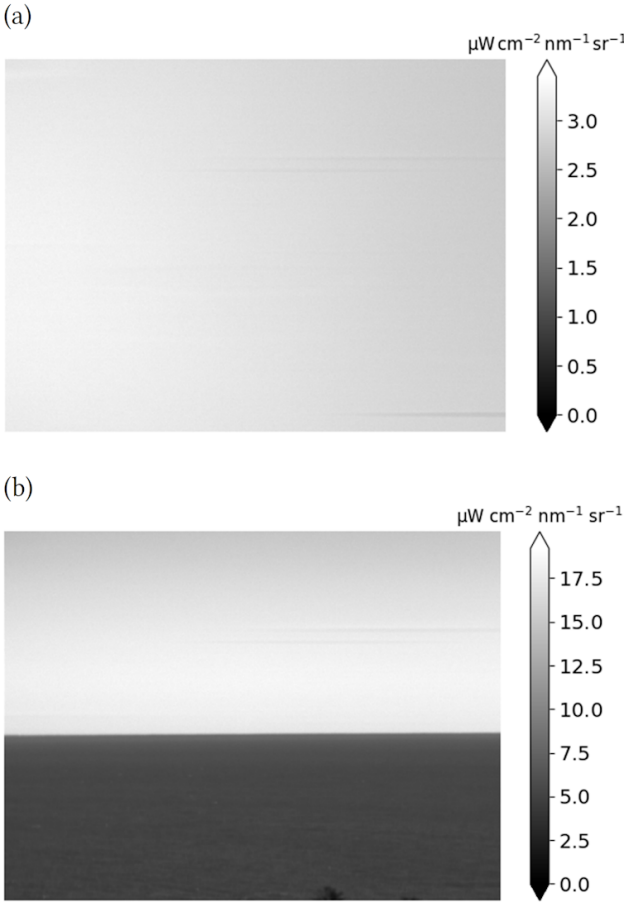

Figure A1. Radiance at 550.8 nm of the clear sky image-cubes acquired on 11 January 2019, in zenith direction at 10:05 LT (a) and looking to the river at 10:11 LT (b).

Appendix B: Comparison of results without an O_4 scaling factor

So far, the comparisons of the O_4 dSCDs between measurements and radiative transfer simulations were made after the O_4 dSCDs derived from the spectral retrieval were multiplied by a scaling factor of 0.8 (see Wagner et al., 2019 and references therein). However, for the cloud-free part of the sky, measurements and simulations can also be brought into agreement if no scaling factor is applied, e.g. for the aerosol extinction profile shown in Fig. B1. For that profile, a larger fraction of the total aerosol amount is located at higher altitudes (e.g. suggested by Ortega et al., 2016). However, for that profile, agreement between measured and simulated radiances is only achieved if an even higher surface albedo of 0.25 is used in the radiative transfer simulations. From these findings, no clear conclusion can be drawn about whether a scaling factor is needed or not. Nevertheless, this ambiguity is not important for the main results of this study.

https://doi.org/10.5194/egusphere-2026-2556
Preprint. Discussion started: 12 June 2026

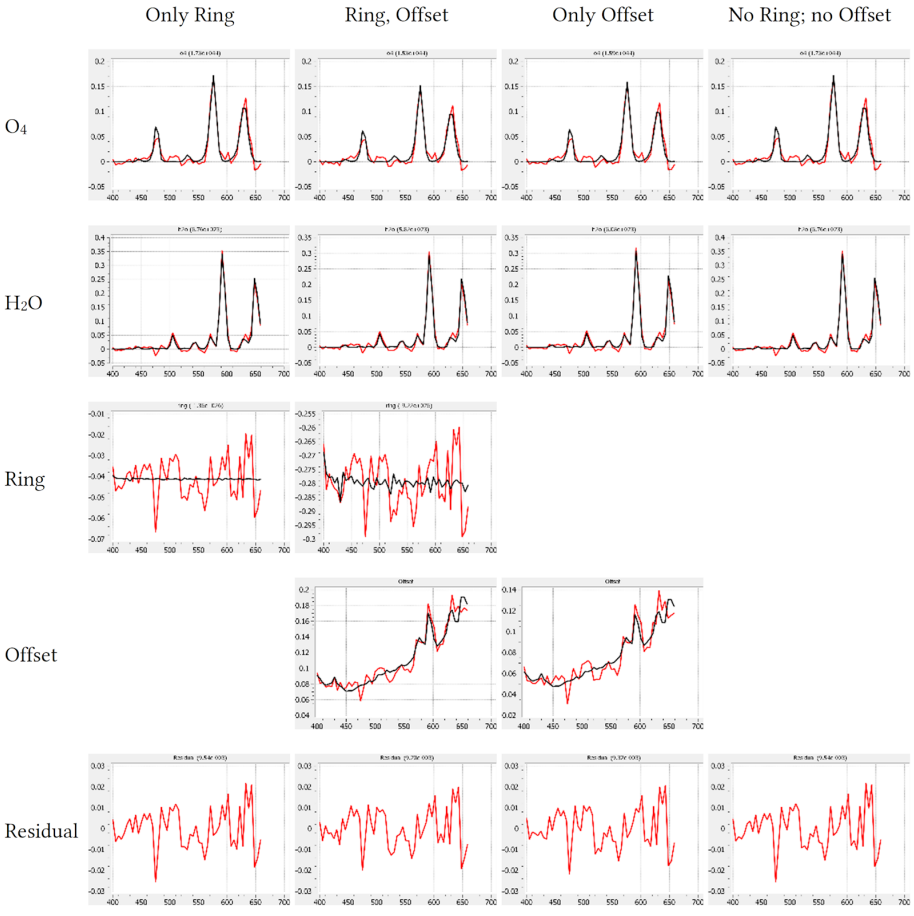

Figure A2. Example of DOAS fit results with different settings. Data was radiometric calibrated.

Appendix C: Backward trajectory simulations

We simulated backward trajectories corresponding to 1 November 2018 around the time of the measurements using HYSPLIT (Stein et al., 2015). The results of these simulartions are presented in Fig. C1 and show that lower altitude air masses reach Montevideo from the southern region of the Atlantic Ocean, while continental air masses at higher altitudes arrive from the east. This supports the interpreation presented in Sect. 5.1.

Author contributions. EF lead the image acquisition instances, instrumental characterization, performed the binning and DOAS analysis of the hyperspectral images, together with several sensibility tests. NC, SD and SZ developed pre-processing and analysis code for manipulation of the hyperspectral files and DOAS results. TW conducted radiative transfer simulations to study the impact of several atmospheric parameters in our results. The manuscript was written by EF and TW with contributions from all coauthors.

https://doi.org/10.5194/egusphere-2026-2556
Preprint. Discussion started: 12 June 2026

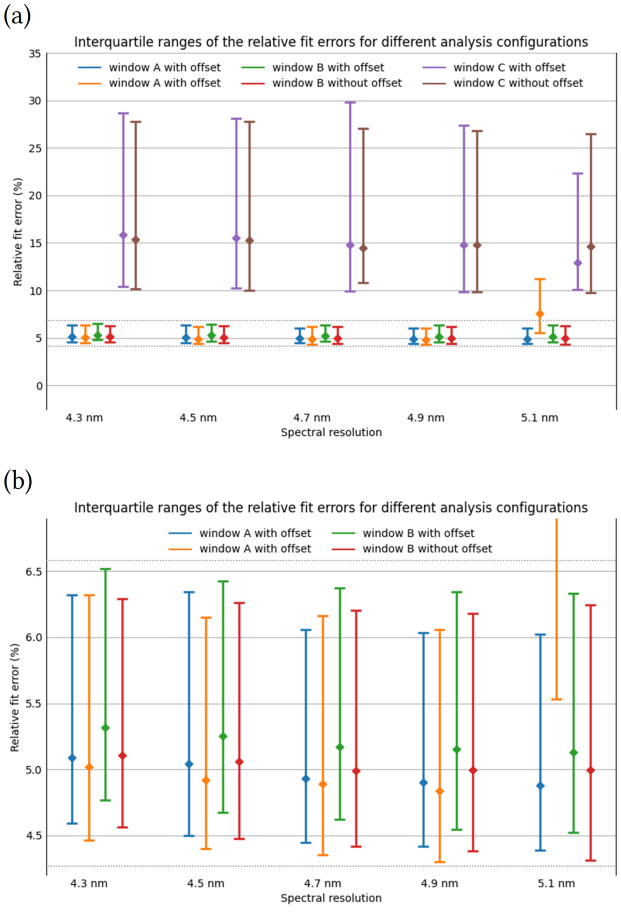

Figure A3. Comparison of the relative errors obtained by the DOAS analysis performed with the settings described in Table A1.

Competing interests. At least one of the (co-)authors is a member of the editorial board of Atmospheric Measurement Techniques. The authors have no other competing interests to declare.

Acknowledgements. EF acknowledges funding by the L'Oreal National Award for Women in Science. EF and NC wish to thank the Programa de Desarrollo de las Ciencias Básicas (PEDECIBA) and the Comisión Sectorial de Investigación Científica (CSIC) for supporting this research. We thank Tim Deutschmann for his efforts in developing the MCARTIM radiative transfer model.

https://doi.org/10.5194/egusphere-2026-2556
Preprint. Discussion started: 12 June 2026

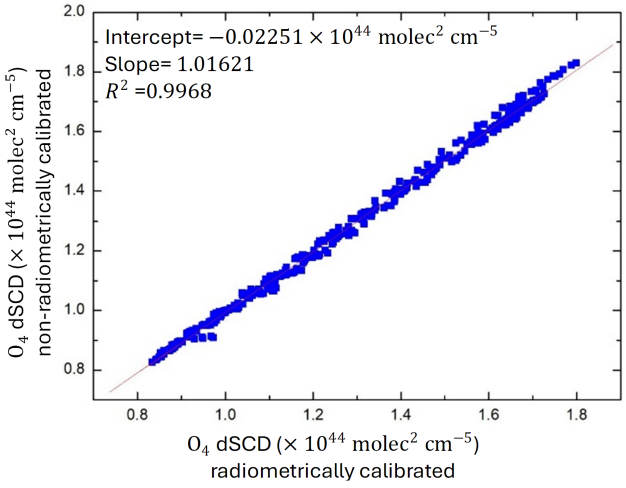

Figure A4. Scatter plot of the results of the sequential analysis for non-radiometrically calibrated spectra compared to radiometrically calibrated spectra

.

References

Bobrowski, N., Hönninger, G., Lohberger, F., and Platt, U.: IDOAS: A new monitoring technique to study the 2D distribution of volcanic gas emissions, Journal of Volcanology and Geothermal Research, 150, 329–338, https://doi.org/10.1016/j.jvolgeores.2005.05.004, 2006.

Bogumil, K., Orphal, J., Homann, T., Voigt, S., Spietz, P., Fleischmann, O. C., A., V., Hartmann, M., Kromminga, H., Bovensmann, H., J., F., Burrows, J. P., and Frerick, J.: Measurements of molecular absorption spectra with the SCIAMACHY pre-flight model: instrument characterization and reference data for atmospheric remote-sensing in the 230-2380 nm region, Journal of Photochemistry and Photobiology A: Chemistry, 157, 167–184, https://doi.org/10.1016/S1010-6030(03)00062-5, 2003.

Borger, C., Beirle, S., Butz, A., Scheidweiler, L. O., and Wagner, T.: High-resolution observations of NO2 and CO2 emission plumes from EnMAP satellite measurements, Environmental Research Letters, 20, 044 034, https://doi.org/10.1088/1748-9326/adc0b1, 2025.

Burrows, J. P., Richter, A., Dehn, A., Deters, B., Himmelmann, S., Voigt, S., and Orphal, J.: Atmospheric remote–sensing reference data from GOME-2. Temperature–dependant absorption cross sections of O3 in the 231–794 nm range, Journal of Quantitative Spectroscopy and Radiative Transfer, 61, 509–517, https://doi.org/10.1016/S0022-4073(98)00037-5, 1999.

Chance, K. and Kurucz, R. L.: An improved high-resolution solar reference spectrum for earth's atmosphere measurements in the ultraviolet, visible, and near infrared, Journal of Quantitative Spectroscopy and Radiative Transfer, 111, 1289–1295, https://doi.org/10.1016/j.jqsrt.2010.01.036, 2010.

Chance, K. and Spurr, R. J.: Ring effect studies: Rayleigh scattering, including molecular parameters for rotational Raman scattering, and the Fraunhofer spectrum., Applied optics, 36, 5224–30, http://www.ncbi.nlm.nih.gov/pubmed/18259337, 1997.

Danckaert, T., Fayt, C., Roozendael, M. V., Smedt, I. D., Letocart, V., Merlaud, A., and Pinardi, G.: QDOAS Software user manual, http://uv-vis.aeronomie.be/software/QDOAS, 2017.

https://doi.org/10.5194/egusphere-2026-2556
Preprint. Discussion started: 12 June 2026

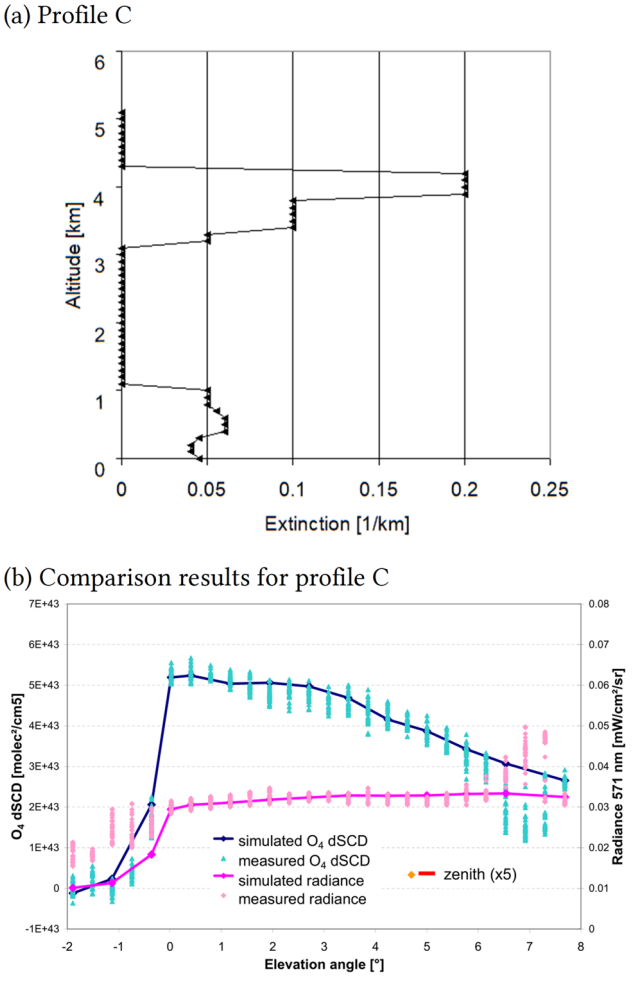

Figure B1. Left: aerosol extinction profile, for which measurements and simulations can be brought into agreement without the application of an O_4 scaling factor. Right: comparison of the measured and simulated radiances and O_4 dSCDs. The blue and magenta dots show the measurement results of the 29 vertical scans of the measurements on 01 November 2018, 15:48. The blue and magenta lines show the corresponding results of the simulations (for the vertical scan in the center of the camera). Also shown are the measured and simulated radiances (indicated by the orange diamond and red bar, respectively) in zenith direction (note that these values are multiplied by 5 to make them better visible).

.

335 Deutschmann, T., Beirle, S., Udo Frieß, Grzegorski, M., Kern, C., Kritten, L., Platt, U., Prados-Román, C., Pukite, J., Wagner, T., Werner, B., and Pfeilsticker, K.: The Monte Carlo atmospheric radiative transfer model McArtim: Introduction and validation of Jacobians and 3D features, Journal of Quantitative Spectroscopy and Radiative Transfer, https://doi.org/10.1016/j.jqsrt.2010.12.009, 2011.

Fayt, C. and Roozendael, M. V.: Software User Manual, http://www.oma.be/BIRA-IASB/Molecules/BrO/WinDOAS-SUM-210b.pdf, 2001.

https://doi.org/10.5194/egusphere-2026-2556
Preprint. Discussion started: 12 June 2026

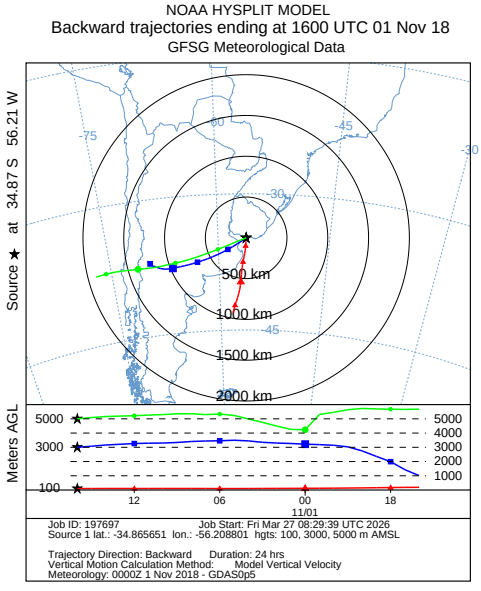

Figure C1. Backward trajectories for 1 November 2018.

.

Hendrick, F., Müller, J.-F., Clémer, K., Wang, P., Mazière, M. D., Fayt, C., Gielen, C., Hermans, C., Ma, J. Z., Pinardi, G., Stavrakou, T., Vlemmix, T., and Roozendael, M. V.: Four years of ground-based MAX-DOAS observations of HONO and NO ₂ in the Beijing area, Atmospheric Chemistry and Physics, 14, 765–781, https://doi.org/10.5194/acp-14-765-2014, 2014.

Hermans, C., Coquart, B., Merienne, M.-F., Colin, R., Jenouvrier, A., Carleer, M., Fally, S., and Vandaele, A. C.: Absorption Cross-section of the Collision-Induced Bands of Oxygen from the UV to the NIR, pp. 193–202, Springer Netherlands, https://doi.org/10.1007/978-94-010-0025-3_16, 2011.

Heue, K.-P., Wagner, T., Broccardo, S. P., Walter, D., Piketh, S. J., Ross, K. E., Beirle, S., and Platt, U.: Direct observation of two dimensional trace gas distributions with an airborne Imaging DOAS instrument, Atmospheric Chemistry and Physics, 8, 6707–6717, https://doi.org/10.5194/acp-8-6707-2008, 2008.

Hönninger, G., von Friedeburg, C., and Platt, U.: Multi axis differential optical absorption spectroscopy (MAX-DOAS), Atmospheric Chemistry and Physics, 4, 231–254, https://doi.org/10.5194/acp-4-231-2004, 2004.

https://doi.org/10.5194/egusphere-2026-2556
Preprint. Discussion started: 12 June 2026

Lee, H., Kim, Y. J., Jung, J., Lee, C., Heue, K.-P., Platt, U., Hu, M., and Zhu, T.: Spatial and temporal variations in NO2 distributions over Beijing, China measured by imaging differential optical absorption spectroscopy, Journal of Environmental Management, 90, 1814–1823, https://doi.org/10.1016/j.jenvman.2008.11.025, 2009.

Lohberger, F., Hönninger, G., and Platt, U.: Ground-based imaging differential optical absorption spectroscopy of atmospheric gases., Applied optics, 43, 4711–7, https://doi.org/10.1364/AO.43.004711, 2004.

Manago, N., Takara, Y., Ando, F., Noro, N., Suzuki, M., Irie, H., and Kuze, H.: Visualizing spatial distribution of atmospheric nitrogen dioxide by means of hyperspectral imaging, Applied Optics, 57, 5970, https://doi.org/10.1364/ao.57.005970, 2018.

Ortega, I., Berg, L. K., Ferrare, R. A., Hair, J. W., Hostetler, C. A., and Volkamer, R.: Elevated aerosol layers modify the O2–O2 absorption measured by ground-based MAX-DOAS, Journal of Quantitative Spectroscopy and Radiative Transfer, 176, 34–49, https://doi.org/10.1016/j.jqsrt.2016.02.021, 2016.

Peters, E., Ostendorf, M., Bösch, T., Seyler, A., Schönhardt, A., Schreier, S. F., Henzing, J. S., Wittrock, F., Richter, A., Vrekoussis, M., and Burrows, J. P.: Full-azimuthal imaging-DOAS observations of NO2 and O4 during CINDI-2, Atmospheric Measurement Techniques, 12, 4171–4190, https://doi.org/10.5194/amt-12-4171-2019, 2019.

Pikelnaya, O., Flynn, J. H., Tsai, C., and Stutz, J.: Imaging DOAS detection of primary formaldehyde and sulfur dioxide emissions from petrochemical flares, Journal of Geophysical Research: Atmospheres, 118, 8716–8728, https://doi.org/10.1002/jgrd.50643, 2013.

Platt, U. and Stutz, J.: Differential Optical Absorption Spectroscopy: Principles and Applications, Springer Verlag, 2008.

Rothman, L. S., Gordon, I. E., Babikov, Y., Barbe, A., Benner, D. C., Bernath, P. F., Birk, M., Bizzocchi, L., Boudon, V., Brown, L. R., Campargue, A., Chance, K., Cohen, E. A., Coudert, L. H., Devi, V. M., Drouin, B. J., Fayt, A., Flaud, J. M., Gamache, R. R., Harrison, J. J., Hartmann, J. M., Hill, C., Hodges, J. T., Jacquemart, D., Jolly, A., Lamouroux, J., Roy, R. J. L., Li, G., Long, D. A., Lyulin, O. M., Mackie, C. J., Massie, S. T., Mikhailenko, S., Müller, H. S., Naumenko, O. V., Nikitin, A. V., Orphal, J., Perevalov, V., Perrin, A., Polovtseva, E. R., Richard, C., Smith, M. A., Starikova, E., Sung, K., Tashkun, S., Tennyson, J., Toon, G. C., Tyuterev, V. G., and Wagner, G.: The HITRAN2012 molecular spectroscopic database, Journal of Quantitative Spectroscopy and Radiative Transfer, 130, 4–50, https://doi.org/10.1016/J.JQSRT.2013.07.002, 2013.

Stein, A. F., Draxler, R. R., Rolph, G. D., Stunder, B. J., Cohen, M. D., and Ngan, F.: NOAA's HYSPLIT Atmospheric Transport and Dispersion Modeling System, Bulletin of the American Meteorological Society, 96, 2059–2077, https://doi.org/10.1175/BAMS-D-14-00110.1, 2015.

Vandaele, A. C., Hermans, C., Simon, P. C., Carleer, M., Colin, R., Fally, S., Mérienne, M. F., Jenouvrier, A., and Coquart, B.: Measurements of the NO2 absorption cross-section from 42 000 cm-1 to 10 000 cm-1 (238–1000 nm) at 220 K and 294 K, Journal of Quantitative Spectroscopy and Radiative Transfer, 59, 171–184, https://doi.org/10.1016/S0022-4073(97)00168-4, 1998.

Wagner, T., Burrows, J. P., Deutschmann, T., Dix, B., von Friedeburg, C., U. Frieß, Hendrick, F., Heue, K.-P., Irie, H., Iwabuchi, H., Kanaya, Y., Keller, J., McLinden, C. A., Oetjen, H., Palazzi, E., Petritoli, A., Platt, U., Postylyakov, O., Pukite, J., Richter, A., van Roozendael, M., Rozanov, A., Rozanov, V., Sinreich, R., Sanghavi, S., and Wittrock, F.: Comparison of box-air-mass-factors and radiances for Multiple-Axis Differential Optical Absorption Spectroscopy (MAX-DOAS) geometries calculated from different UV/visible radiative transfer models, Atmospheric Chemistry and Physics, 7, 1809–1833, https://doi.org/10.5194/acp-7-1809-2007, 2007.

Wagner, T., Beirle, S., Benavent, N., Bösch, T., Chan, K. L., Donner, S., Dörner, S., Fayt, C., Udo Frieß, García-Nieto, D., Gielen, C., González-Bartolome, D., Gomez, L., Hendrick, F., Henzing, B., Jin, J. L., Lampel, J., Ma, J., Mies, K., Navarro, M., Peters, E., Pinardi, G., Puentedura, O., Pukite, J., Remmers, J., Richter, A., Saiz-Lopez, A., Shaiganfar, R., Sihler, H., Roozendael, M. V., Wang, Y., and Yela, M.: Is a scaling factor required to obtain closure between measured and modelled atmospheric O4 absorptions? An assessment

https://doi.org/10.5194/egusphere-2026-2556
Preprint. Discussion started: 12 June 2026

of uncertainties of measurements and radiative transfer simulations for 2 selected days during the MAD-CAT campaign, Atmospheric Measurement Techniques, 12, 2745–2817, https://doi.org/10.5194/AMT-12-2745-2019, 2019.

Wagner, T., Dörner, S., Beirle, S., Donner, S., and Kinne, S.: Quantitative comparison of measured and simulated O4 absorptions for one day with extremely low aerosol load over the tropical Atlantic, Atmospheric Measurement Techniques, 14, 3871–3893, https://doi.org/10.5194/amt-14-3871-2021, 2021.

Wagner, T., Warnach, S., Beirle, S., Bobrowski, N., Jost, A., Puķīte, J., and Theys, N.: Investigation of three-dimensional radiative transfer effects for UV–Vis satellite and ground-based observations of volcanic plumes, Atmospheric Measurement Techniques, 16, 1609–1662, https://doi.org/10.5194/amt-16-1609-2023, 2023.

Wittrock, F., Oetjen, H., Richter, A., Fietkau, S., Medeke, T., Rozanov, A., and Burrows, J. P.: MAX-DOAS measurements of atmospheric trace gases in Ny-Ålesund- Radiative transfer studies and their application, Atmospheric Chemistry and Physics, 4, 955–966, https://doi.org/10.5194/ACP-4-955-2004, 2004.